# Autoencoder-assisted study of directed percolation with spatial long-range interactions

Yanyang Wang,[1] Yuxiang Yang,[1] and Wei Li[1]

[1]*Key Laboratory of Quark and Lepton Physics (MOE) and Institute of Particle Physics, Central China Normal University, Wuhan 430079, China*

In the field of non-equilibrium phase transitions, the classification problem of reaction-diffusion processes with long-range interactions is both challenging and intriguing. Determining critical points serves as the foundation for studying the phase transition characteristics of these universality classes. In contrast to Monte Carlo simulations of statistical system observables, machine learning methods can extract evolutionary information from clusters of such systems, thereby rapidly identifying phase transition regions. We have developed a new method that uses one-dimensional encoded results of the stacked autoencoder to determine critical points, and it has a high level of reliability. Subsequently, the critical exponent $\delta$ of particle survival probability and the characteristic time $t_f$ of finite-scale systems can be measured. Utilizing the scaling relation $t_f{\sim}L^z$ yields the dynamic exponent $z$. Finally, we discuss an alternative method adopting Lévy distribution to generate random walk steps, inserting another global expansion mechanism. The critical points obtained through it are very close to the predictions of field theory. This study suggests promising applications of autoencoder methods in processes involving such long-range interactions.

## I. INTRODUCTION

In recent years, machine learning has been widely applied in various fields of physics[1]. With the powerful mapping and generalization capabilities of neural networks, both supervised and unsupervised learning have found numerous applications. Examples include astronomy[2–4], quantum information[5–7], high-energy physics[8–10], biophysics[11–14], and complexity science[15, 16].The research methods related to complexity and critical phenomena include but are not limited to, mean-field theory, renormalization, exact diagonalization [17, 18], and numerical simulation methods such as Monte Carlo (MC) simulations[19–21]. Machine learning can be involved in both the theoretical and numerical solution processes of phase transition models, greatly enriching the solution approaches and the scope of their applications. For equilibrium systems, statistical methods based on general ensemble theory are well established[22]. However, the prevalence of open systems in nature forces us to consider the dynamical behavior of non-equilibrium systems. The dialectical relationship between equilibrium and non-equilibrium systems informs us about the applicability of theoretical methods such as mean-field theory and field theory renormalization in non-equilibrium phase transition models[23–26]. It also inspires us to explore the possibility of combining MC simulations and machine learning for numerical solutions[27].

Machine learning has made significant progress in some equilibrium phase transition models[28–30]. For non-equilibrium phase transitions, the absence of detailed balance allows for richer critical behavior in systems that are far from equilibrium. Absorbing phase transitions are a class of continuous phase transitions in non-equilibrium systems, where the transition occurs between an absorbing state with no surviving particles and an active state with active particles, controlled by a series of reaction-diffusion processes in the particle dynamics evolution. An important universality class of absorbing phase transitions is the directed percolation(DP) university class, characterized by consistent critical exponents and exemplified by the DP model. The measurement of a series of critical exponents is a vital reference for determining the universality class to which a model belongs. Within the theoretical approaches, the DP universality is identified by several fundamental conditions[31, 32]. In a broader context of particle reaction-diffusion, the DP universality class is observed in branching-annihilating random walks(BAW) processes with an odd number of branches[33, 34]. Conversely, the BAW models with an even number of branches belong to the parity-conserving(PC) universality class[35–37]. The use of supervised and unsupervised machine learning methods to study the critical properties of non-equilibrium phase transition models appears to offer promising applications and research potential[38–40]. Among these approaches, unsupervised learning methods provide a way to extract features near the critical point of a system[41–44].

One of the conditions for ensuring the robustness of the directed percolation (DP) universality class is to guarantee that the system only exhibits local interactions in both time and space, which aligns with the consideration of reactions and diffusion involving only nearest-neighbor particles in processes such as DP and BAW model. However, when considering the coupling of interactions and potential distributions in a lattice model, bringing in long-range interactions into reaction-diffusion systems can better reflect real physical systems. Taking into account Lévy-like flights in DP may alter its universality class, and it may find broader applications under conditions such as long-range infection, latent periods, and memory effects in realistic scenarios[45]. In the context of epidemic spread, Mollison proposed an extension of directed percolation with non-local spreading mechanisms[46], where diseases spread over a distance of $r$ in a $d$-dimensional space, with $r$ following a typical power-law distribution

$$P(r)\sim\frac{1}{r^{d+\sigma}}\sim\frac{1}{r^{\beta}}. \tag{1}$$

The random walk displacement that satisfies this algebraic distribution is known as Lévy-like flights [47]. Levy-like flights have a shorter time scale compared to the nearest-neighbor propagation models, resulting in non-local effects and longer distance extensions. In the analysis of probability density evolution for particle random walk models, Lévy flights can be generated by introducing nonlinear operators, also known as fractional order derivatives[48]. In our numerical simulation approach, we incorporate long-range interactions in the reaction-diffusion process through the settings of random numbers and step sizes. We discuss the relevant simulation details of introducing Lévy-like flights into the DP model at the spatial scale, predict critical points, and measure several critical exponents, based on the the DP model with spatial long-range interactions.

Utilizing unsupervised learning to identify and predict the structural characteristics of the evolution of phase transition models is one of the fundamental methods in applying machine learning to study phase transition[38]. Stacked autoencoders (SAE), which combine fully connected neural networks and autoencoders, are one type of unsupervised learning algorithm. The primary objective of an autoencoder, involving an encoder, decoder, and loss function, is data dimensionality reduction and reconstruction. The learning process of an autoencoder can be regarded as the minimization of a loss function. Fully connected neural networks, on the other hand, provide a data compression method when dealing with grid-like structured data. When employed as a supervised learning algorithm, fully connected neural networks can effectively identify critical states of some phase transition models[27]. The basic structure of SAE involves gradually stacking fully connected layers in the encoding and decoding processes. In practice, the structural details of SAE often need adjusting according to the system size. We consider the potential of utilizing SAE in the encoding process to identify critical states of spatial Lévy-like flights in the DP process, aiming to explore the feasibility of applying unsupervised learning methods based on autoencoders to study the critical properties of long-range interaction non-equilibrium phase transition models in the context of (1+1)-dimensional spatial Lévy-like flights DP models.

The structure of this paper is as follows: In Sec.II, we introduce the specific definition of the DP with spatial Lévy-like flights (LDP) model and briefly review the general results of mean-field theory and renormalization group analysis based on field theory. In Sec.III.A, we discuss the simulation details of introducing spatial long-range interactions into the DP model and present some numerical simulation results of the evolution. In Sec.III.B, we outline the general process of SAE methods and discuss how certain settings affect the training process. Sec.IV.A provides a series of predicted critical points based on the one-dimensional encoding output using SAE. In Sec.IV.B, we observe the decay behavior of the system's particle density at these critical points to determine the critical exponent $\delta$. Furthermore, in Sec.IV.C, we investigate the growth of active particles at critical points to determine the characteristic time $t_f$ of finite-scale systems, thereby obtaining the measured value of the dynamic exponent $z$. SAE can effectively identify these characteristic times. Finally, in Sec.IV.D, we use the measured values of the critical exponents to verify the compliance of the scaling relationship (7) and study the impact of a new method for generating random walk step sizes on critical points. In Sec.V, we summarize this work and provide an outlook on future research directions.

## II. FIELD THEORY APPROACH TO DP WITH SPATIAL LÉVY-LIKE FLIGHTS

In the framework of particle reaction-diffusion, the continuous phase transition from an active state to an inactive state in a system demonstrates that the dynamic evolution of such absorbing phase transitions is truly a non-equilibrium process influenced by fluctuations. In order to investigate the probability distribution analysis of non-equilibrium system structures, it is necessary to abandon the detailed balance condition and the Einstein relation that controls the long-time evolution direction of the system in setting up the dynamics equations for such systems [49–51]. The renormalization analysis of the DP model with spatial Lévy-like flights is based on the construction of the action.

Before discussing the results of renormalization group analysis based on field theory, analyzing the mean-field approximation method that neglects high-dimensional fluctuation effects can provide insight into the dimensions and relevant scaling characteristics where system fluctuations are important. The ordinary mean-field equation for ordinary DP considering only nearest-neighbor interactions is[31]

$$\frac{\partial}{\partial t}n(\mathbf{x},t)=\left(\tau+D_N\nabla^2\right)n(\mathbf{x},t)-\lambda n^2(\mathbf{x},t)+\zeta(\mathbf{x},t), \tag{2}$$

where $n(\mathbf{x},t)$ is the density of active particles, and $\nabla^2$ represents the nearest-neighbor diffusion operator. For bringing in the long-range interactions and extending reaction-diffusion to the entire system, we consider Lévy-like flights with a power-law distribution, where the random walk distance $r$ follows a spatially long-range decay according to distribution (1).The extension of equation (2) to DP models with long-range interactions requires the introduction of a nonlinear operator for non-local integration. The mean-field equation for the LDP is given by

$$\frac{\partial}{\partial t}n(\mathbf{x},t) = \left(\tau + D_A\nabla^\sigma + D_N\nabla^2\right)n(\mathbf{x},t) - \\ -\lambda n^2(\mathbf{x},t) + \zeta(\mathbf{x},t), \tag{3}$$

where $\nabla^\sigma$ describes the non-local reaction-diffusion behaviour, and the operator $\nabla^\sigma$ is known as a fractional-order derivative, characterized by its properties as follows:

$$\nabla^\sigma e^{i\vec{k}\cdot\vec{r}} = -|\vec{k}|^\sigma e^{i\vec{k}\cdot\vec{r}}. \tag{4}$$

Through the mean-field approximation analysis, they obtained the upper critical dimension $d_c = 2\sigma = 4$, marking the crossover of the anomalous DP and ordinary DP controlled by the critical parameter. Contrasting the $\nabla^2$ term representing the ordinary DP diffusion mechanism in the evolution equation, they found that the $\nabla^\sigma$ term controls the non-local reaction-diffusion behavior of the anomalous DP. Regarding the critical exponents $\nu_\parallel$ and $\nu_\perp$, when $\sigma > 2$, they transition to the universal class of ordinary DP, and the mean-field results indicate that $\nu_\perp$ varies continuously.

Below the upper critical dimension, it is necessary to fully consider the system's fluctuation effects. Field-theoretic renormalization group (RG) methods can provide predictions for the critical exponents of such reaction-diffusion systems. By utilizing the expression of equation (3) within a bosonic multiparticle system, we can obtain a coherent state path integral representation of the pseudo-Hamiltonian. Through the extension of the continuum limit, an effective action is derived as follows:

$$S[\bar{\psi},\psi] = \int d^dx dt \left[\bar{\psi}\left(\partial_t - \tau - D_N\nabla^2 - D_A\nabla^\sigma\right)\psi + \\ +\frac{g}{2}\left(\bar{\psi}\psi^2 - \bar{\psi}^2\psi\right)\right]. \tag{5}$$

The effective action serves as the foundation of quantum field theory, allowing for the analysis of higher-order diagrams using Feynman diagram methods and the determination of critical exponents through RG approaches. The paper [52], calculations were conducted for the $d = 2\sigma - \epsilon$ dimensional space DP with Lévy-like flights using dimensional regularization-based renormalization methods, providing predictions for critical exponents under the one-loop diagram approximation. Some of the results are as follows:

$$\begin{aligned} \nu_\perp &= \frac{1}{\sigma} + \frac{2\epsilon}{7\sigma^2} + O\left(\epsilon^2\right), \\ \nu_\parallel &= 1 + \frac{\epsilon}{7\sigma} + O\left(\epsilon^2\right), \\ z = \frac{\nu_\parallel}{\nu_\perp} &= \sigma - \epsilon/7 + O\left(\epsilon^2\right), \\ \delta &= 1 - \frac{3\epsilon}{7\sigma} + O\left(\epsilon^2\right). \end{aligned} \tag{6}$$

Due to the correlation between the upper critical dimension and $\sigma$, by selecting specific parameter values, it may be possible to verify one-loop order results near the upper critical dimension. Specifically, we are interested in the scaling relation

$$\frac{1}{\delta} - \frac{\beta - 2}{\delta} z = 2, \tag{7}$$

where $\beta = \sigma + d$. While critical components $\nu_\parallel, \nu_\perp$ vary continuously, $\beta$ governs the crossover between the anomalous DP and ordinary DP. By inserting the critical components of ordinary DP [53] [20, 23, 24] into equation (7), they obtain the value of critical control parameter $\beta_c = 3.0776(2)$ in one spatial dimension. In numerical work, we attempt to compare theoretical results by taking a series of different $\beta$ values. Additionally, we seek to compare the conditions for generating some of the critical exponents of ordinary DP by using different methods for generating random walk steps.

## III. MODEL AND AUTOENCODER METHOD

### A. Simulation of the DP with spatial Lévy-like flights

By setting the transition probabilities within the Domany-Kinzel automaton (DK), the update rules for the ordinary (1+1)-dimensional DP process can be determined. The basic setup of the DK cellular automaton model involves using the occupation status of surrounding lattice points to determine the occupation state of a lattice point at the next time step. For the ordinary DP, the occupation state of the point $s_{i,t}$ depends only on its nearest neighbors $s_{i-1,t}$ and $s_{i+1,t}$. The update rules for bond DP can be expressed as:

$$s_{i,t+1} = \begin{cases} 1 & \text{if } s_{i-1,t} \neq s_{i+1,t} \quad \text{and } z_i(t) < p, \\ 1 & \text{if } s_{i-1,t} = s_{i+1,t} = 1 \text{ and } z_i(t) < p(2-p), \\ 0 & \text{otherwise }, \end{cases} \tag{8}$$

where $s_{i,t+1} = 1$ represents a site being occupied, and $s_{i,t+1} = 0$ represents a site not being occupied. $z_i(t)$ is a uniformly distributed random number in the interval $[0, 1]$, and $p$ is an artificially set hyperparameter representing the transition probability.

A general way to introduce the space Lévy-like flights into the ordinary DP process described above is to change the influences on the state occupied by the locus at the next moment. This entails replacing the nearest neighbors $s_{i-1,t}$ and $s_{i+1,t}$ with $s_{i-[L],t}$ and $s_{i+[R],t}$, where $[L]$ and $[R]$ represent the largest positive integers not exceeding the distances $L$ and $R$, respectively. In this case, the

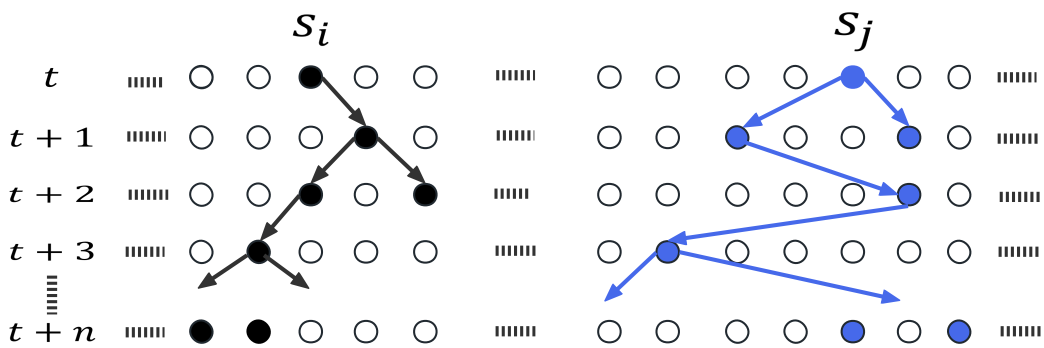


FIG. 1. The evolution of (1+1)-dimensional ordinary DP and LDP. In the following illustrations, black and blue dots represent occupied sites, while empty dots indicate unoccupied sites. The left panel depicts the evolution rules (8) for ordinary DP, with black particles evolving over time steps starting from $S_i$ following the black arrows. The blue dots represent an example of the evolution of LDP at $S_j$ according to rules (9). Unlike ordinary DP, the interaction range of LDP is not limited to nearest neighbors, allowing particles to appear further apart in a shorter period of time.

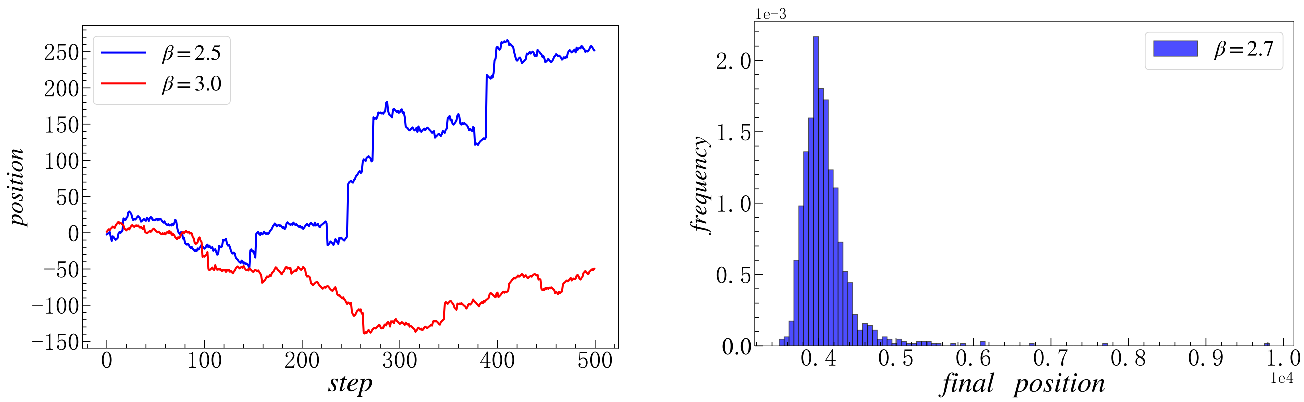


(a) (b)

FIG. 2. (a) A one-dimensional random walk conducted based on the step sizes generated according to formula (10) for $\beta = 2.5, = 3.0$. The horizontal axis represents the number of steps in the random walk, while the vertical axis indicates the position of the particle at the current step. It can be observed from the graph that larger step sizes can be generated for smaller $\beta$ values. In (b), with the number of steps set to 2000, a distribution plot of the final positions of particles after 1000 independent random walks is shown. The horizontal axis represents the final positions where particles appear, and the vertical axis represents the corresponding frequency of those positions. It is evident from the graph that there are pronounced characteristics of a long-tailed distribution.

update rules for LDP can be expressed as:

$$s_{i,t+1} = \begin{cases} 1 & \text{if } s_{i-[L],t} \neq s_{i+[R],t} \quad \text{and } z_i(t) < p, \\ 1 & \text{if } s_{i-[L],t} = s_{i+[R],t} = 1 \text{ and } z_i(t) < p(2-p), \\ 0 & \text{otherwise .} \end{cases} \tag{9}$$

When setting the generation rules for $L$ and $R$, different forms of spatial long-range interactions can be introduced. Figure 1 represents the evolution of ordinary DP and LDP, where the percolation action of the blue points is not limited to the nearest neighboring lattice points. We are considering the spatial long-range interactions that follow power-law distributions. It's worth noting that there are multiple methods for generating random walk step sizes that satisfy power-law distributions, and in this part, we have employed

$$\begin{aligned} [L] &= Max(L), L = Z_L^{-1/(\beta-1)}, \\ [R] &= Max(R), R = Z_R^{-1/(\beta-1)}. \end{aligned} \tag{10}$$

to define the generation rule of step size. Here, the function $Max(L)$ denotes the maximum integer not exceeding $L$, while $Z_L, Z_R \in (0,1)$ are random numbers following a uniform distribution. $\beta$ is a positive real number greater than 1. It can be verified that $L$ and $R$ conform to a normalized probability distribution[54].

$$P(r) = \begin{cases} \frac{\beta-1}{r^\beta}, & \text{if } \quad \beta > 1, \\ 0, & \quad \text{otherwise .} \end{cases} \tag{11}$$

At $\beta = 2.0, 3.0$, we generate 500 steps for one-dimensional random wandering, as shown in Figure 2(a).

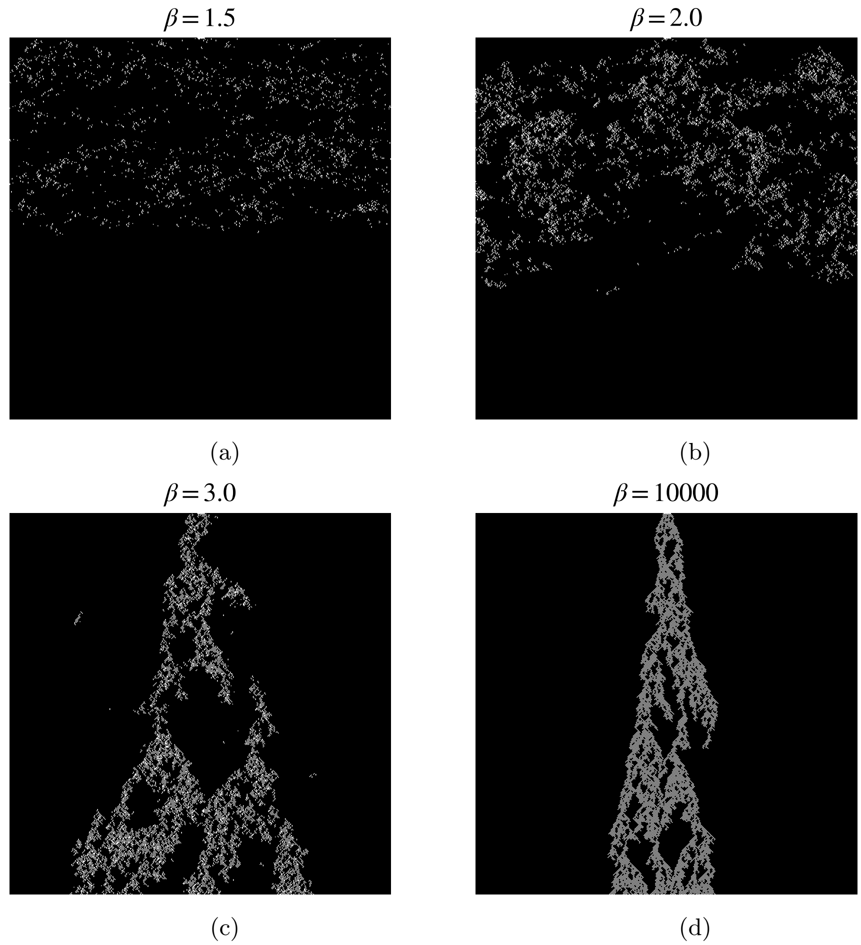


FIG. 3. The clusters growth structure starting from an initial set of 10 active seeds for $\beta = 1.5, 2, 3, 10000$, with a system size of $L = 500$ and a time step setting of $t = 500$. When $\beta$ is small, the system may transition to the absorbing state more rapidly, indicating a decrease in the characteristic time of system evolution, and clusters tend to become more dispersed. As $\beta$ increases, the system evolution leads to the formation of larger clusters and a more ordered structure. When $\beta = 10000$, the cluster growth structure closely resembles the evolution of ordinary DP.

From the figure, it can be observed that $\beta$ is smaller, it is possible to generate larger step sizes. In addition, Figure 2(b) shows the distribution of step lengths for 2000 random walks, from which an obvious "long-tailed distribution" can be seen. The diffusion of particles from the site $s_i$ at time $t$ to the site at time $t+1$ depends on the generation of step sizes $[L]$ and $[R]$. We employ the $Max$ function to ensure that interactions cover the entire lattice. For example, particles at position $s_i$ can diffuse to$s_{i-[L]}, s_{i-[L-1]}, ..., s_i, s_{i+1}, s_{i+2}, ..., s_{i+[R-1]}, s_{i+[R]}$.

We implemented a simulation program in Python7 to simulate the evolution rules of LDP, utilizing periodic boundary conditions to reduce finite-size effects. In Figure 3, we present the growth results of clusters under different $\beta$ values. When $\beta$ is small, the system is more likely to quickly enter an absorbing state, indicating a smaller characteristic time and a tendency for clusters to disperse. As $\beta$ increases, the system forms larger clusters with a more ordered structure. From the perspective of system fluctuations, increasing $\beta$ tends to enhance the influence of fluctuations, leading to an increase of the upper critical dimension, consistent with the field theory prediction of $d_c = 2(\beta - 1)$.

### B. Method of Stacked Autoencoder

Different from traditional supervised learning methods, unsupervised learning may be capable of predicting the critical properties of absorbing phase transitions. In the absence of any prior information about the system's dynamic evolution, the objective of unsupervised learning can be to provide the probability distribution of random vectors [42, 43]. Among these methods, autoencoders, as a mature unsupervised learning approach, have been applied in the study of phase transitions and critical phenomena. An autoencoder is a type of neural network with the fundamental training objective of attempting to replicate the input to the output or perform incomplete input replication. By setting different loss functions, the encod-

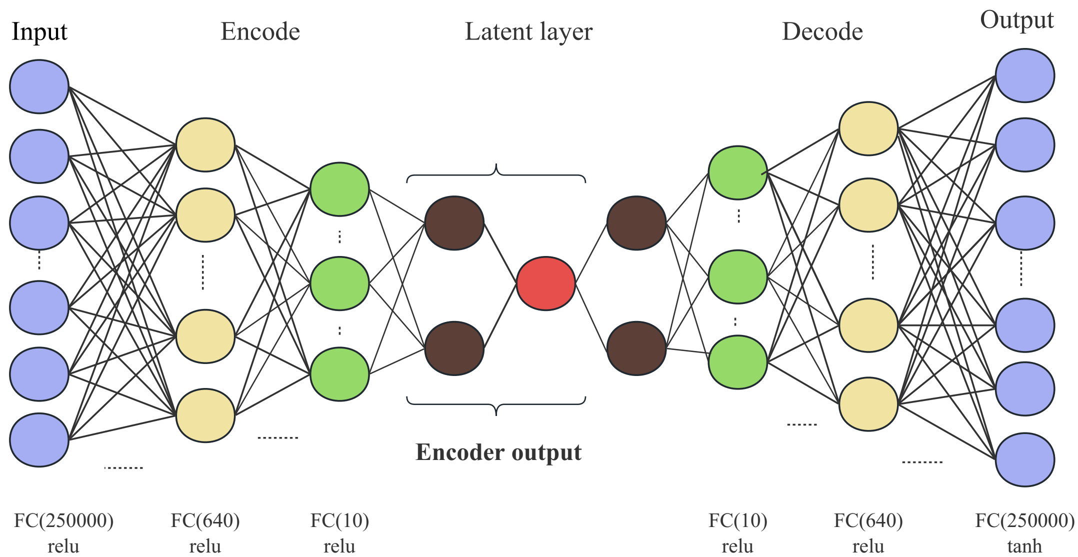


FIG. 4. The general structure of an SAE is designed with layered hidden units to preserve the original cluster graph information as much as possible. The Encoder output section in the figure is extracted after the training of the SAE. Two brown-colored neurons are used to analyze structural features, while one red-colored neuron is used to determine the critical point.

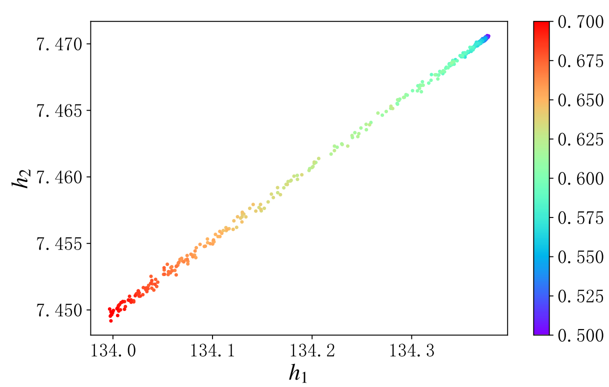


FIG. 5. Two-dimensional feature extraction of $(1+1)$-dimensional LDP training by SAE.The right color bars represent different values of directed percolation probabilities. When approaching the critical point, the points show the characteristics of fuzzy dispersion.

ing and decoding effectiveness of the autoencoder can be evaluated. Considering the effectiveness of autoencoders in handling image data, we attempted to use an autoencoder with a fully connected neural network structure to process cluster configuration of absorbing phase transitions. Given the particular LDP model near the critical point, our basic approach is to utilize the dimensionality reduction function of the autoencoder to extract the spatial and temporal structural characteristics of the system's cluster configurations and compare the characteristic outputs under different percolation probabilities to determine the position of the critical point.

We designed a SAE structure based on a fully connected neural network, and Figure 4 illustrates the encoding and decoding processes of the autoencoder. We chose mean squared error (MSE) as the loss function to assess the data reconstruction capability of the autoencoder. During the encoding and decoding processes, we used multiple hidden layers to preserve the structural information of the initial data as much as possible and employed dynamic learning rates to optimize the model's parameter configuration. In the parameter updating process, we utilized the Adam optimizer to introduce momentum-corrected biases and introduced regularization to weaken training noise. Finally, we extracted the hidden variables encoded to the specified dimension.

Our basic workflow for using SAE generally includes the following steps. Firstly, we fix the value of the hyper-parameter $\beta$. Cluster graphs with different percolation probabilities, as shown in Figure 3, are fed into the SAE, corresponding to the 'Input' layer in Figure 4. Similar to the left part of Figure 4, the SAE then encodes the original data through fully connected layers with gradually decreasing neurons and applies the ReLU activation function to provide non-linear mapping. After encoding, the original input data is dimensionally reduced, and the dimensionality is determined by specifying the number of neurons in the 'Encoder output' layer.

Decoding is the reverse process of encoding, aiming to reshape the original cluster graph using the low-dimensional results obtained through encoding. After multiple backpropagation and parameter updates, mean squared error is used as the loss function to evaluate the data reconstruction performance. Once SAE training is complete, we retain the encoding results with different numbers of neurons. The results of two neurons correspond to the positions of brown points in Figure 4, while the result of one neuron corresponds to the position of

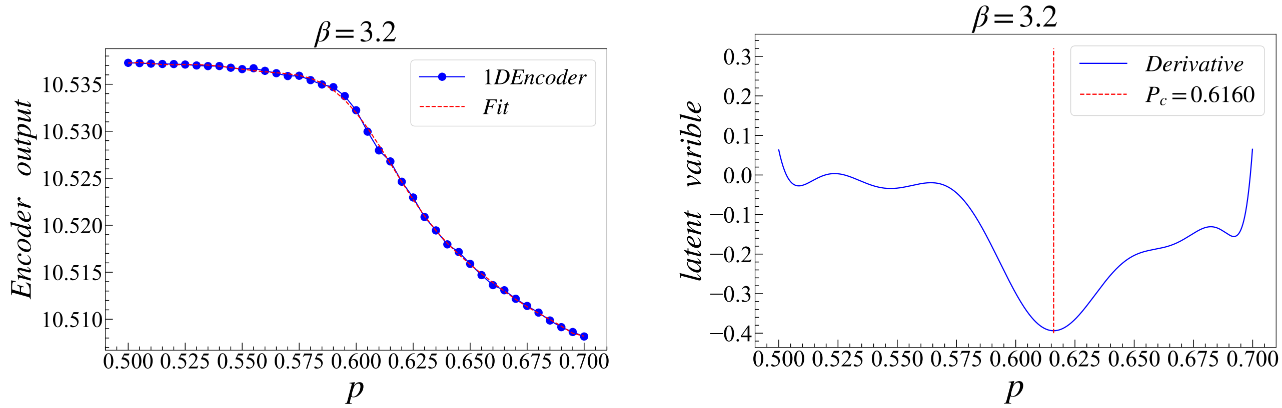


(a) (b)

FIG. 6. At $\beta = 3.2$, the one-dimensional encoding output of the hidden layer in SAEs, and the determination of the LDP critical point $P_c$. (a) For a system size of 500 and a time step of 500, we obtained the one-dimensional output of SAEs for 41 percolation probability $p$ in the range of $[0.50, 0.70]$. The blue dots represent the one-dimensional encoding output of SAEs, while the red dashed line represents the result of polynomial fitting. Under the settings of Figure (a), the derivative of the fitted result of the one-dimensional encoding output of SAEs is shown by the blue curve in (b). By identifying the global minimum in the extreme value of the derivative curve, we determined the position of the system's critical point characterized by the percolation probability $P_c = 0.6160$.

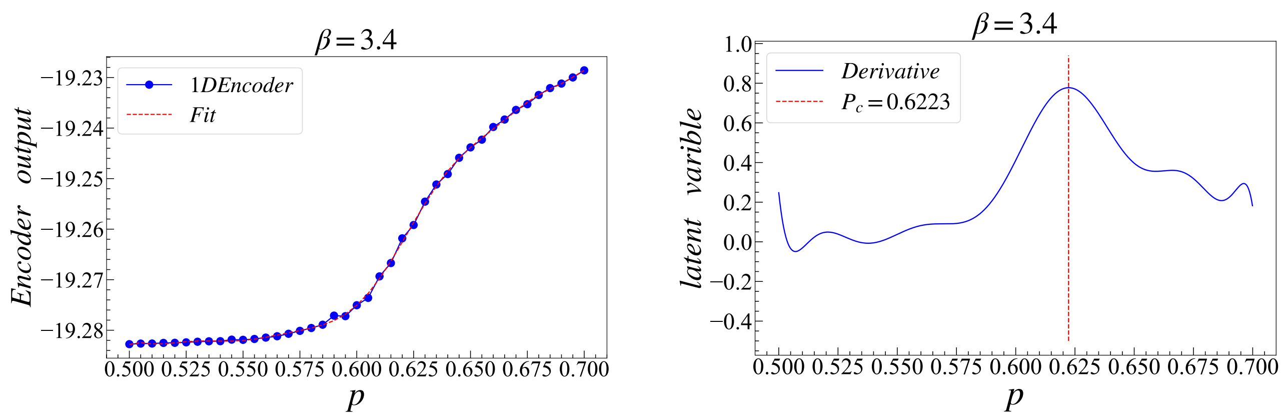


(a) (b)

FIG. 7. At $\beta = 3.4$, the one-dimensional encoding output of the hidden layer in SAEs, and the determination of the LDP critical point $P_c$. The system settings are consistent with those in Figure 6. Due to the non-uniqueness of the monotonicity of the fitted results of the one-dimensional encoding output of autoencoders, with different values of $\beta$, the critical point can be determined based on the characteristics of extremum in its derivative curve. According to the global maximum value of extremum in Figure (b), the system's critical point is identified as $P_c = 0.6223$.

the red point in Figure 4. As shown in Figure 5, we use different colors to label the results of the two neurons. The result of one neuron is represented by a single color, such as the blue circle in Figure 6(a).

## IV. AUTOENCODER AND NUMERICAL RESULTS

### A. Determination of critical points

We initially employ an autoencoder to extract and analyze the two-dimensional features of cluster configurations from the LDP model. Considering training costs and precision, we select 41 $p$ values at intervals of 0.005 within the range of $[0.5, 0.7]$. For each $p$, we repeatedly generate cluster configuration, resulting in a training set of $41{\times}500$ cluster configurations and a test set of $41{\times}50$ cluster configurations. The system size is $L = 500$ , the time step is set to $t = 500$ , and the value of the hyper-parameter $\beta$ is chosen to be 3.2 firstly.

To retain as much cluster diagram structural information as possible, we employ full-seed initial conditions. By setting the hidden layer to be two-dimensional, we extract the two-dimensional structural features of the cluster configuration, as illustrated in Figure 5. In the

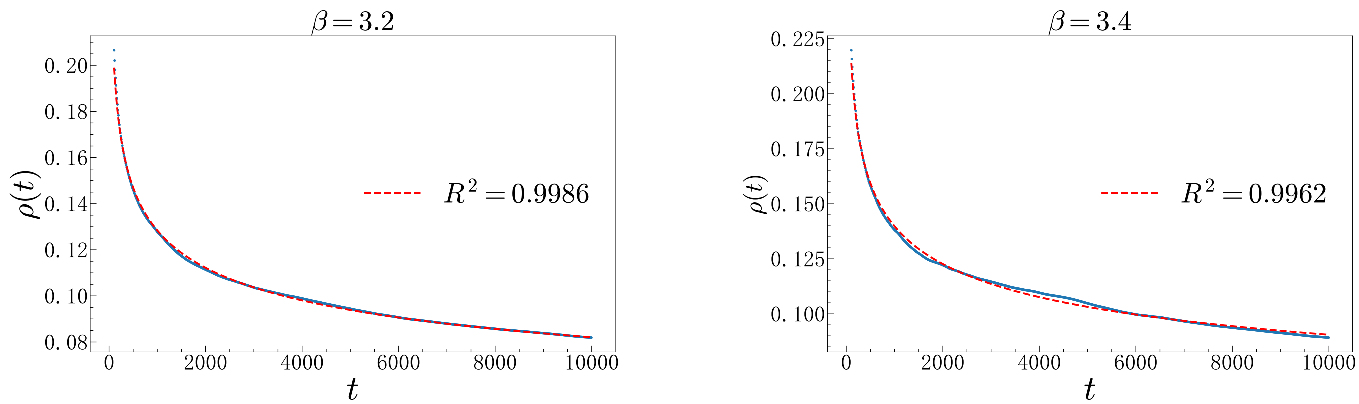


(a) (b)

FIG. 8. (a) At $\beta = 3.2$ and $p = 0.6160$, the decay of the system's active particle density and the goodness of fit. The system size is $L = 10000$, and the time step is set to $t = 10000$. The red dashed curve represents the function curve fitted using a power-law, and the definition of goodness of fit is described in the text, with a resulting $R^2 = 0.9986$.(b) At $\beta = 3.4$ and $p = 0.6223$, the decay of the system's active particle density and the goodness of fit. The system size and time step settings are the same as in (a), with a goodness of fit of $R^2 = 0.9962$. The optimal value of $R^2$ is 1, and we believe that this method of determining the critical point is highly reliable.

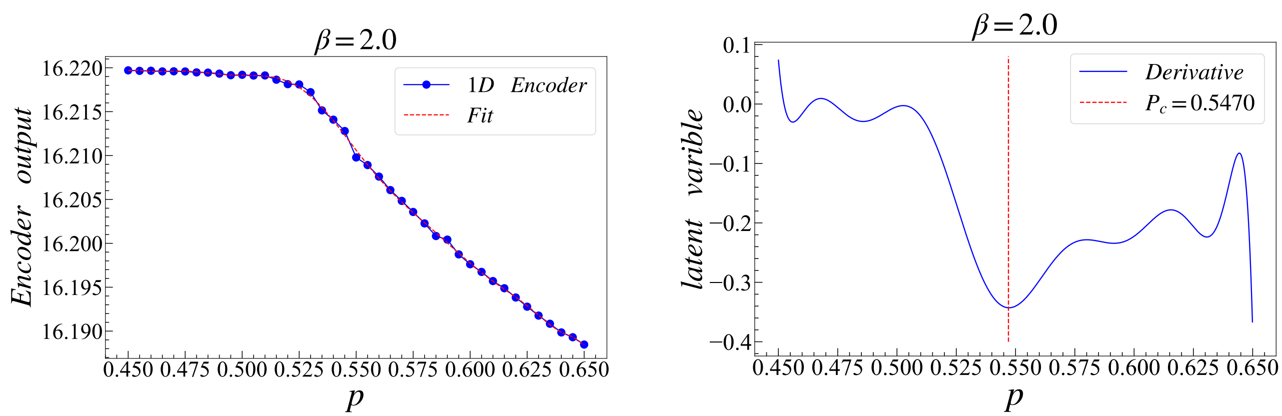


(a) (b)

FIG. 9. To investigate the relationship between the critical point and the hyperparameter $\beta$, we measured a set of numerical values for the critical point $P_c$ corresponding to different $\beta$. Taking $\beta = 2.0$ as an example, Figure (a) displays the one-dimensional encoding output of stacked autoencoders and the polynomial fitting results, while Figure (b) illustrates the critical point determined by the derivative curve, with $P_c = 0.5470$. We summarize the other results in Table I.

figure, $h1$ and $h2$ represent the coordinates of the two-dimensional feature points, and the color bar on the right indicates the corresponding colors for different branching probability values. The results indicate that near the critical point, the feature points are blurred and dispersed, even fractured, suggesting that the autoencoder has captured the particularities near the critical point of the system. We infer that the autoencoder can distinguish the power-law growth characteristics of particle density near the critical point and specific structural features of the cluster configuration from regions far from the critical point. Based on this idea, we set the hidden layer to be one-dimensional and identify the critical point through the features of the one-dimensional data.

We select $\beta = 3.2, 3.4$ and input the corresponding training and test sets into the autoencoder, obtaining the results of the autoencoder's extraction of one-dimensional features from the cluster diagrams, as shown in Figure 6(a) and Figure 7(a). Observing the features of the curves in Figure 6(a) and Figure 7(a), when $p \to P_c^{theoretical}$, the curves appear to reach maximum curvature. Therefore, we perform a polynomial fitting of the curves and plot the relationship between the derivative of the fitted curve and $p$. The results are depicted in Figure 6(b) and Figure 7(b). We find that the global minimum or maximum in the extreme values in the figures corresponds to the percolation probability, which can be used as our estimate for $P_c$. According to the results in Figure 6(b) and Figure 7(b), when $\beta = 3.2$ and 3.4, we estimate their corresponding critical points to be $P_c = 0.6160$ and

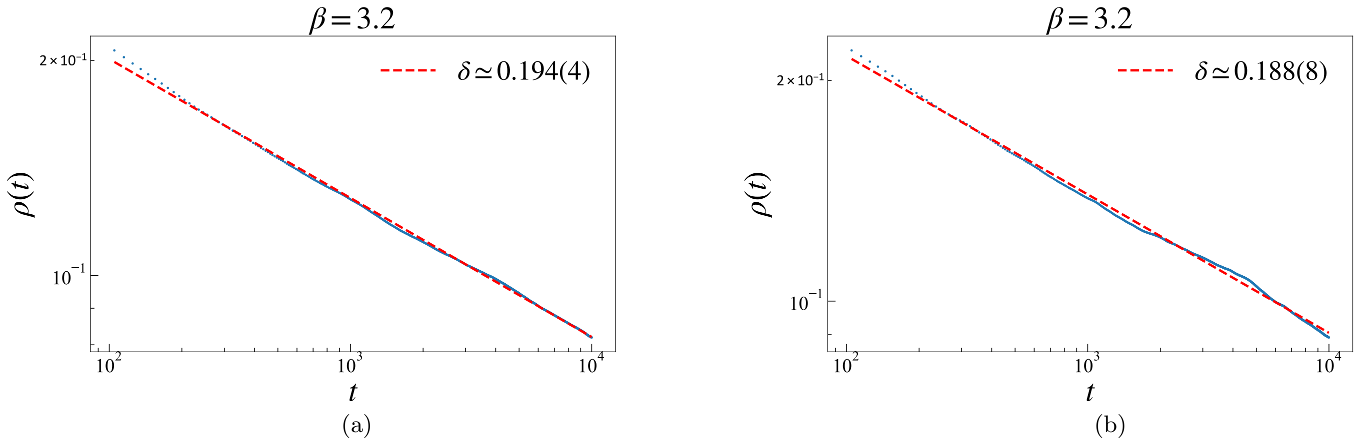


FIG. 10. The measurement of the critical exponent $\delta$ is conducted with the system settings identical to those in Figure 8. (a) At $\beta = 3.2$, we present the decay of active particle density at the critical point $P_c = 0.6160$ in a double-logarithmic coordinate system. According to Equation 12, the critical exponent is estimated as $\delta \simeq 0.194(4)$. (b) At $\beta = 3.4$, the value of the critical exponent $\delta$ at the critical point $P_c = 0.6223$ is determined to be 0.188(8).

0.6223. To examine the feasibility of such an approach, we counted the decay of the particle density of the system with $\beta = 3.4, 3.6$ . The decay form of the active particle density at the critical point is

$$\rho(t) \sim t^{-\delta}. \tag{12}$$

We performed a power-law fit to the particle density, where the results in ordinary coordinates are shown in Fig. 8. We also calculated the goodness of fit

$$R^2 = 1 - \frac{\sum (y_a - y_p))^2}{\sum (y_a - y_m)^2}, \tag{13}$$

where $y_a$ represents the statistically measured actual density, $y_p$ represents the predicted values corresponding to the fitted curve, and $y_m$ represents the mean value of the actual measurements. When $\beta = 3.4$ and 3.6, the goodness of fit $R^2 = 0.9986$ and 0.9962, respectively. Considering that the optimal value for $R^2$ is 1, we believe that this method of determining the critical point of the system has a high level of credibility.

To investigate the relationship between the critical point and the hyperparameter $\beta$, we duly select a series $\beta$ to measure $P_c$. At $\beta = 3.6, 3.4, 3.2, 3.0, 2.8, 2.6, 2.4, 2.2$, we select 41 $p$ as percolation probabilities at intervals of 0.005 within the range of $[0.5, 0.7]$ to generate training and test sets. Similarly, at $\beta = 2.0, 1.8, 1.6, 1.4, 1.2$, we choose 41 $p$ within the range of $[0.45, 0.65]$. Additionally, we measured the critical point at the crossover $\beta_c = 3.0766$ between anomalous DP and ordinary DP predicted by the field-theoretic RG. As an example, Figure 9 illustrates the representative results at $\beta = 2.0$. All the measurements of $P_c$ are summarized in Table I.

### B. Measurement of critical exponent $\delta$

In the above work, we are also able to estimate the density decay exponent $\delta$ of the system particles. To reduce statistical errors, we measured the particle density decay of larger-sized systems based on the critical points determined by the autoencoder. Specifically, we initially observed the variation in particle density for system sizes of $L = 10000$ and time steps of $t = 10000$ at $\beta = 3.2, 3.4$ with $P_c = 0.6160, 0.6223$. To mitigate the impact of random errors, we averaged the results of the evolution with 100 different initial conditions. As an example, the results of $\delta$ obtained through linear fitting in double-logarithmic coordinates are depicted in Figure 10. The fitting result for Figure 10(a) is $0.49195837t^{-0.19448102}$, and for Figure 10(b) it is $0.51525595t^{-0.18883931}$. Subsequently, we measured the values of the density decay exponent $\delta$ at $\beta = 3.6, 3.077(6), 3.0, 2.8, 2.6, 2.4, 2.2, 2.0, 1.8, 1.6, 1.4, 1.2$ corresponding to the critical points $P_c$ in Table I. The summary of all measurements of the critical exponent $\delta$ is presented in Figure 11(b) and Table I.

Regarding the measurement of critical points in 11(a), we obtained different values of $P_c$ for various $\beta$, suggesting that $P_c$ in the LDP model continuously varies based on the hyperparameter $\beta$. The variation of the critical exponent $\delta$ indicates that, under the control of $\beta$, the system deviates from the universality class of ordinary DP. This demonstrates that the introduction of long-range interactions alters the symmetry of the ordinary DP system.

### C. Measurement of the dynamic exponent $z$

For verifying *exact* scaling relation (7), we attempt to calculate system dynamical exponent $z$, which, at the

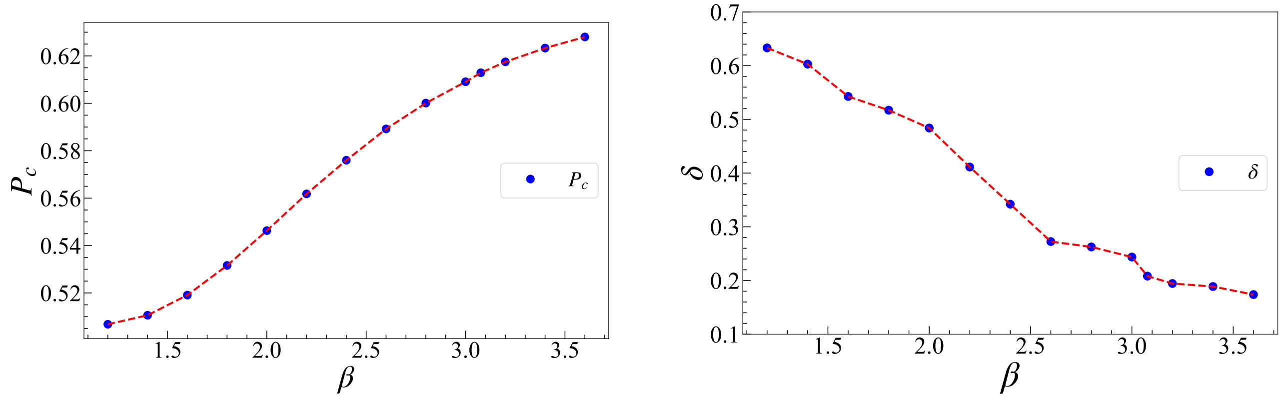


(a) (b)

FIG. 11. A set of critical points $P_c$ and critical exponents $\delta$ corresponding to different values of $\beta$. (a) The variation of critical points corresponding to different values of $\beta$ (specific values are provided in the text). It can be inferred that the critical points undergo continuous changes under the control of the parameter $\beta$. (b) The variation of the critical exponent $\delta$ at different values of $\beta$. Due to the significant dependence of $\delta$ measurement on statistical averaging, increasing the measurement cost may yield smoother results. However, based on Figure (b), it can still be inferred that the critical exponent $\delta$ exhibits continuous changes with the parameter $\beta$.

| $\beta$ | 1.2 | 1.4 | 1.6 | 1.8 | 2.0 | 2.2 | 2.4 | 2.6 | 2.8 | 3.0 | 3.077(6) | 3.2 | 3.4 | 3.6 |
|---|---|---|---|---|---|---|---|---|---|---|---|---|---|---|
| $P_c$ | 0.5068 | 0.5106 | 0.5191 | 0.5316 | 0.5470 | 0.5618 | 0.5760 | 0.5892 | 0.6000 | 0.6091 | 0.6129 | 0.6160 | 0.6223 | 0.6280 |
| $\delta$ | 0.6331 | 0.6029 | 0.5427 | 0.5171 | 0.4839 | 0.4113 | 0.3421 | 0.2725 | 0.2825 | 0.2537 | 0.2082 | 0.1944 | 0.1888 | 0.1738 |

TABLE I. A set of critical points corresponding to $\beta$ and the critical exponent $\delta$ obtained through statistical measurements of the system's active particle density.

critical point, obeys the scaling relation

$$\xi_\perp \sim t^{\frac{1}{z}}. \tag{14}$$

And $\xi_\perp$ refers to spatial correlation length. Considering the relation between dynamical exponent $z$ and mean square spreading exponent $\widetilde{z}$, where $\widetilde{z} = 2/z$, and $\widetilde{z}$ satisfies the scaling relation

$$r^2(t) \sim t^{\widetilde{z}}. \tag{15}$$

It is common to measure mean square spreading $r^2$ of surviving clusters from origin in place of the dynamical exponent $z$. However, simulations have shown that $r^2$ does not exhibit a power-law but diverges at the critical point in the presence of long-range interaction[54]. In a finite lattice system, there is a non-vanishing probability of reaching the absorbing configuration. In the critical region, when the spatial size of the system is $L$, the system reaches an absorbing state after a characteristic time $t_f$, which satisfies the relation:

$$t_f \sim L^z. \tag{16}$$

We utilize finite-size effects to determine the dynamic exponent $z$. In brief, we record the time steps required for systems of multiple sizes to reach an absorbing configuration at critical probability. We then perform a fitting on those time steps to determine $z$.

Due to computational limitations, the upper time step limit set in our simulations is not smaller than the characteristic time of ordinary DP universality classes. The introduction of long-range interactions leads to the clustering structure becoming more discrete, and the absorbing state appearing more quickly. Compared to ordinary DP, such systems have a smaller dynamic exponent when $\beta$ is small. We selected five system sizes ($L = 60, 65, 70, 75, 80$) for each value of $\beta = 2.2, 2.4, 2.6, 2.8, 3.0, 3.2, 3.4, 3.6$ and performed finite-size scaling analysis with a temporal scale limit of $1200, 1400, 1600, 1800, 2000$ for each system size. To reduce random errors, we performed five times ensemble averages for a total of 25000 systems for each system size. Figure 12(a) displays the characteristic time $t_f$ and its standard deviation obtained from ensemble averages of systems with $\beta = 3.6$ and $L = 60$. The small standard deviation can serve as a reference for measuring accuracy. Based on the power-law relationship between the characteristic time and finite size, we fitted the $t_f$ for different system sizes and calculated the dynamical exponent $z = 1.5765(4)$, as shown in Figure12(b). The dynamical exponents for other values of $\beta$ are listed in TableII.

We find that both $z$ and $t_f$ decrease as $\beta$ decreases. To distinguish the measured values of $t_f$ for different finite sizes and reduce the system error, we increased

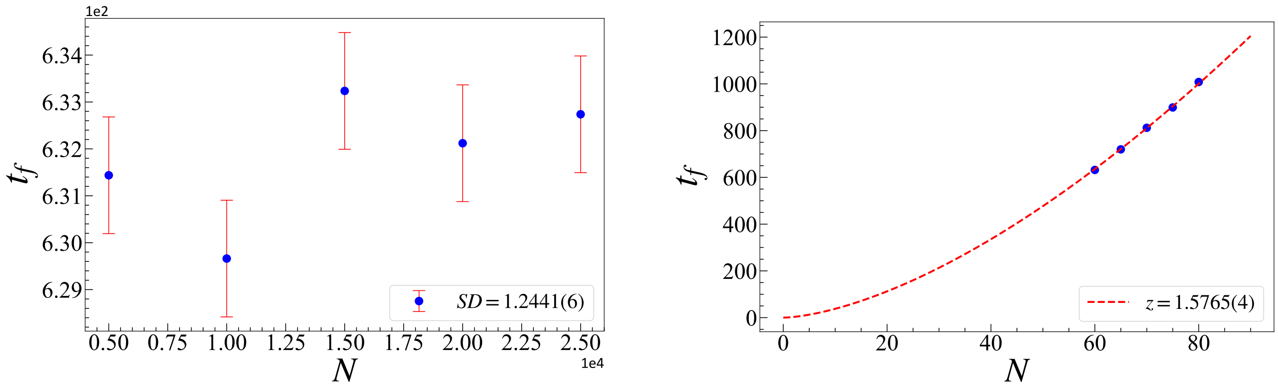


(a) (b)

FIG. 12. At $\beta = 3.6$, the standard deviation of characteristic times for systems with the same size and the measurement of the critical exponent $z$ for systems with different sizes. (a) For $L = 60$ and $t = 1200$, the average values of $t_f$ taken every 5000 steps are computed, and the standard deviation of these five measurements is calculated as $SD = 1.2441$. (b) System sizes $L = 60, 65, 70, 75, 80$ with corresponding time step settings of $1200, 1400, 1600, 1800, 2000$, respectively, are used to calculate the statistical values of characteristic times, with each $t_f$ being the result of averaging over 25000 statistical measurements. Utilizing the relationship (16) between characteristic times and dynamic exponent $z$, the critical exponent is determined as $z = 1.5765(4)$.

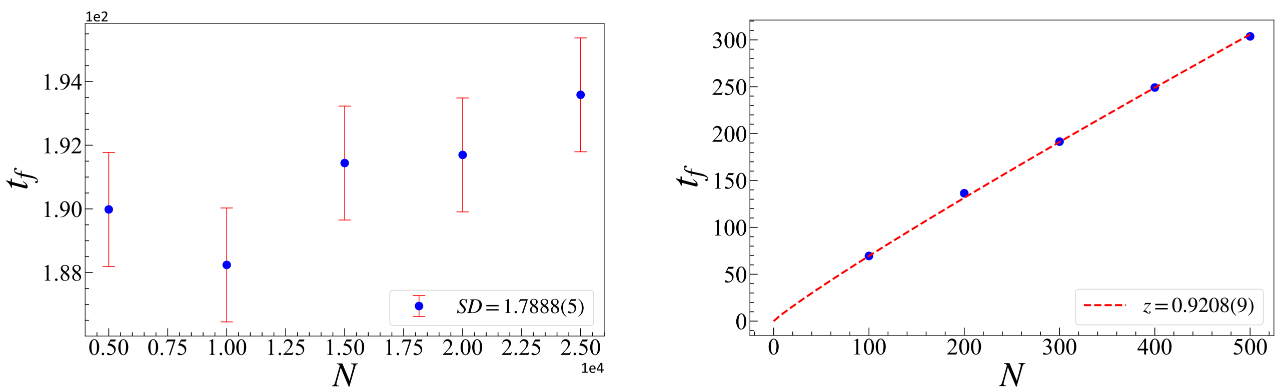


(a) (b)

FIG. 13. At $\beta = 1.8$, the standard deviation of characteristic times for systems with the same size and the measurement of the critical exponent $z$ for systems with different sizes. (a) For $L = 300$ and $t = 600$, the average values of $t_f$ taken every 5000 steps are calculated, and the standard deviation of these five measurements is computed as $SD = 1.7888$. (b) The statistical values of characteristic times for system sizes $L = 100, 200, 300, 400, 500$ with corresponding time step settings of $200, 400, 600, 800, 1000$, respectively, are shown. Each $t_f$ represents the result of averaging over 25000 statistical measurements. The fitted result for the critical exponent $z$ is $z = 0.920(8)$.

the system's spatial scale($L = 100, 200, 300, 400, 500$) for $\beta = 1.2, 1.4, 1.6, 1.8, 2.0$. At the same time, to reduce simulation costs, we decreased the temporal scale limit of the system($t = 200, 400, 600, 800, 1000$). In Figure 13, we show the measured value of $t_f$ and the fitted value of $z$ for $\beta = 1.8, L = 300, t = 600$. Figure 14(a) displays the curve of $z$ for $\beta$.

After obtaining the above results, we used the cluster diagrams generated at different time scales as both training and testing inputs for an autoencoder. Our aim was to observe the one-dimensional hidden layer output in order to capture the critical evolution characteristics of the system. For example, under the conditions of $\beta = 3.4$ and $P_c = 0.6223$, we generated cluster configurations at different temporal scales for system size $L = 60$, with the temporal scale ranging from $t \in [550, 590]$. We generate a total of $41 \times 500$ cluster configurations as the training set and select 1/10 of them as the testing set input into the autoencoder. Figure 14(b) demonstrates the results of the single latent layer variables. It is evident that the latent variable increases suddenly near the characteristic time, indicating that the autoencoder is also capable of recognizing critical features of the system.

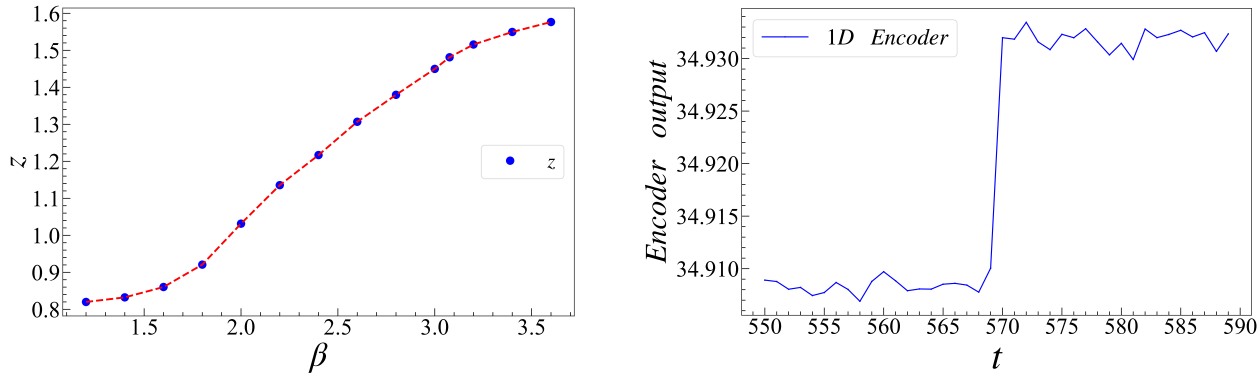


FIG. 14. (a) Measurements of the dynamic exponent $z$ corresponding to a set of $\beta$ values (specific values are provided in the text) suggest that the dynamic exponent continuously changes with the parameter $\beta$. Combining the measurements of the critical exponents $\delta$ and $\Theta$ mentioned above, indicates that the universality class to which the DP system belongs under spatial Lévy-like long-range interactions dynamically changes with the parameter $\beta$. (b) At $\beta = 3.4$ and $P_c = 0.6223$, for a system of size $L = 60$, the one-dimensional encoding output after training with stacked autoencoders for cluster plots at different time steps is presented. The presence of larger gaps in the plot, particularly those close to the predicted characteristic time $t_f = 569.40$, indicates that stacked autoencoders can effectively recognize this evolutionary feature of the system.

| $\beta$ | 1.2 | 1.4 | 1.6 | 1.8 | 2.0 | 2.2 | 2.4 | 2.6 | 2.8 | 3.0 | 3.077(6) | 3.2 | 3.4 | 3.6 |
|---|---|---|---|---|---|---|---|---|---|---|---|---|---|---|
| $z$ | 0.819(9) | 0.832(3) | 0.860(3) | 0.920(8) | 1.031(5) | 1.13(5) | 1.216(9) | 1.306(9) | 1.379(7) | 1.449(8) | 1.481(2) | 1.515(7) | 1.549(6) | 1.5765(4) |

TABLE II. By statistically analyzing characteristic times for systems of different sizes but the same $\beta$, and fitting to obtain the values of the dynamic exponent $z$.

### D. Validation of a scaling form

Thus far, we have obtained the critical points and critical exponents, $\delta$ and $z$, for multiple values of $\beta$. We attempted to compare the theoretical values of $\delta$ with the numerical simulation results in one-dimensional space. Referring to the scaling form 7, $\delta$ can be expressed as

$$\delta = \frac{1}{2}\left(1 - \frac{\beta - 2}{z}\right). \tag{17}$$

It can be seen that the measured values are in good agreement with the theoretical values for $\beta \in [2.0, 2.6]$ in Figure15. However, for other values of $\beta$, the measured values deviate from the theoretical calculations. There may be several reasons for this. Firstly, when $\beta$ is small, the reaction diffusion distance of the system particles is relatively large, and the particles have more opportunities to survive outside of the finite system. Therefore, finite size effects have a significant impact, resulting in a large deviation in the measurement of the critical point and critical exponents. Secondly, due to the intersection of ordinary DP and anomalous DP, there is a difference in the critical exponents of the two methods when $\beta_c = 3.077(6)$. Calculations of the higher-order diagrams based on the renormalization group may yield results that are more consistent with the simulation. Until $\beta = 3.6$, the measured value of the dynamic exponent $z = 1.5765(4)$ is close to the dynamic exponent $z_{OrdinaryDP} = 1.5807(4)$ of ordinary DP. Modifying the method for generating random walk step sizes may lead to measurement results that are more consistent with the theoretical calculations. Considering the specific math form of the Lévy distribution, we tried a method of generating a random walk step length that conforms to the Lévy distribution [55]. The step length $s$ is generated by the following equation

$$s = \frac{u}{|v|^{1/(\beta' - 1)}}, \tag{18}$$

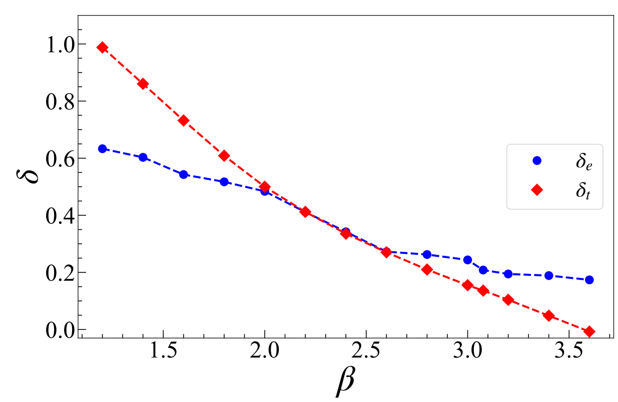


FIG. 15. Comparison between the measured and theoretical values of the critical exponent $\delta$, where $\delta_e$ represents the experimentally measured value, and $\delta_t$ is the theoretically calculated value based on Equation 17.

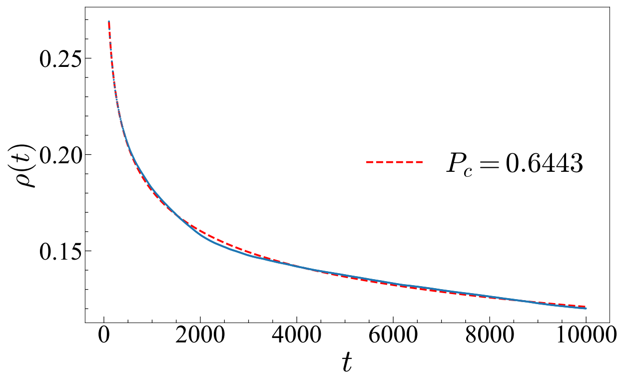


FIG. 16. At $\beta' = 3.0$, the measurement of the critical point is conducted by introducing a global expansion mechanism using the Lévy distribution to generate random walk step lengths. The obtained critical point is very close to the critical point of the ordinary DP, $P_c = 0.6447$.

where $u, v$ follow normal distribution

$$u \sim N(0, \sigma_u^2), \qquad u \sim N(0, \sigma_v^2). \tag{19}$$

Besides,

$$\sigma_u = \left\{ \frac{\Gamma(\beta') \sin(\pi(\beta' - 1)/2)}{\Gamma(\beta'/2)(\beta' - 1)2^{(\beta'-2)/2}} \right\}^{1/(\beta'-1)}, \quad \sigma_v = 1. \tag{20}$$

Based on the above rules, we repeatedly generated 2000 random step lengths at $\beta' = 2.0, 3.0$. The generated step sizes follow a power-law distribution $L(s) \sim |s|^{-\beta'}, 1 < \beta' \leq 3$. We replaced the step sizes $L$ and $R$ in Sec.III. A, and measured the critical point of the system, at $\beta' = 3.0$, to be $P_c = 0.6443$, which is closer to the critical point of ordinary DP, $P_c^{OrdinaryDP} = 0.6447$, as shown in Figure 16. However, this updating rule can only generate random walks with $\beta' \in (1, 3]$, and optimizing it may yield more complete results, which can be compared with the results from the renormalization group.

## V. CONCLUSION

We investigated the (1+1)-dimensional DP model with power-law distributed, spatial long-range interacting variables using autoencoders and MC methods. We determined the critical points of the system for different hyperparameters $\beta$, measured some critical exponents, and attempted to compare the results with those from field theory and the renormalization group.

The results of the cluster diagram indicate that spatial long-range interactions alter the ordered structure of the system, enhancing the influence of fluctuations and thereby modifying the upper critical dimension of the model. Using a SAE, we identified the critical points of the system controlled by the hyperparameter $\beta$. Based on the one-dimensional encoded results of the SAE. We find that the maximum or minimum value in the extreme values of the curve derivative can characterize the location well where the critical point is located. Additionally, we calculated the goodness of fit $R^2 = 0.9986, 0.9962$ between the numerical results of particle density and the theoretically predicted power-law decay form, demonstrating the high credibility of this unsupervised learning approach. Subsequently, we record the variations in critical points of the system corresponding to different $\beta$ values, as shown in Figure 11 and Table I. We infer that in the DP system with spatial long-range interactions, the critical point $P_c$ undergoes continuous changes with the parameter $\beta$.

To explore the universality class to which the DP system with such Lévy-like spatial long-range interactions belongs, we measured the critical exponents $\delta$ and $z$ of the system. The results indicate that the universality class of the DP system with Lévy-like flights spatial long-range interactions changes with the hyperparameter $\beta$. In particular, we compared the compliance of the scaling relation (7) in different $\beta$ intervals. The results show that only when $\beta \in [2.0, 2.6]$ do the numerical results match well with the field theory results. We speculate that this defect is caused by the finite-size effect and the updating rule of the random walk steps, so we used a new steps updating rule for numerical simulations. We found that $\beta' = 3.0$ yields a critical point very close to that of the ordinary DP, which is consistent with the predictions of field theory. Since this algorithm can only generate step lengths in the range of $\beta' \in (1.0, 3.0]$, we expect to make reasonable modifications to the algorithm or design new methods to generate random walk step lengths that comply with the power-law distribution. In addition, introducing different forms of long-range interactions in space and time may broaden the application of DP evolution mechanisms. In conclusion, we have expanded the application of autoencoders, an unsupervised learning method, in reaction-diffusion systems with long-range interactions, providing a valid reference for combining machine learning with other numerical simulation methods to solve cutting-edge problems.

## VI. ACKNOWLEDGEMENTS

This work was supported in part by the Key Laboratory of Quark and Lepton Physics (MOE), Central China Normal University(Grant No.QLPL2022P01), the National Natural Science Foundation of China (Grant No. 11505071, 61702207 and 61873104), and the 111 Project, with Grant No. BP0820038.

[1] I. Goodfellow, Y. Bengio, and A. Courville, *Deep learning* (MIT press, 2016).

[2] E. A. Huerta, G. Allen, I. Andreoni, J. M. Antelis, E. Bachelet, G. B. Berriman, F. B. Bianco, R. Biswas, M. Carrasco Kind, K. Chard, *et al.*, Nature Reviews Physics **1**, 600 (2019), doi:10.1038/s42254-019-0097-4.

[3] S. Andrianomena, Journal of Cosmology and Astroparticle Physics **2022** (2022), doi:10.1088/1475-7516/2022/10/016.

[4] M. J. Smith and J. E. Geach, Royal Society Open Science **10**, 221454 (2023), doi:10.1098/rsos.221454.

[5] Y.-C. Ma and M.-H. Yung, npj Quantum Information **4**, 1 (2018), doi:10.1038/s41534-018-0081-3.

[6] A. Kookani, Y. Mafi, P. Kazemikhah, H. Aghababa, K. Fouladi, and M. Barati, "Xpookynet: Advancement in quantum system analysis through convolutional neural networks for detection of entanglement," (2023), arXiv:2309.03890 [quant-ph].

[7] X.-M. Zhang, W. Kong, M. U. Farooq, M.-H. Yung, G. Guo, and X. Wang, Physical Review A **103** (2021), 10.1103/physreva.103.l040403.

[8] H. Erbin and A. H. Fırat, "Characterizing 4-string contact interaction using machine learning," (2022), doi:10.48550/arXiv.2211.09129, arXiv:2211.09129 [hep-th].

[9] F. Ma, F. Liu, and W. Li, Phys. Rev. D **108**, 072007 (2023).

[10] J. Steinheimer, L.-G. Pang, K. Zhou, V. Koch, J. Randrup, and H. Stoecker, Journal of High Energy Physics **2019**, 1 (2019), doi:10.1007/JHEP12(2019)122.

[11] Y. Jian, C. Zeng, and Y. Zhao, "Direct information reweighted by contact templates: Improved rna contact prediction by combining structural features," (2017), doi:10.48550/arXiv.1711.10674, arXiv:1711.10674 [q-bio.BM].

[12] Q. Yan, Y. Zheng, S. Jia, Y. Zhang, Z. Yu, F. Chen, Y. Tian, T. Huang, and J. K. Liu, "Revealing fine structures of the retinal receptive field by deep learning networks," (2020), doi:10.1109/TCYB.2020.2972983, arXiv:1811.02290 [q-bio.NC].

[13] A. Tareen and J. B. Kinney, arXiv preprint arXiv:2001.03560 (2019), doi:10.1101/835942.

[14] M. Giulini and R. Potestio, Interface focus **9**, 20190003 (2019).

[15] Z. K. Maseer, R. Yusof, B. Al-Bander, A. Saif, and Q. K. Kadhim, arXiv preprint arXiv:2308.02805 (2023).

[16] R. Xie and M. Marsili, "A simple probabilistic neural networks for machine understanding," (2023), arXiv:2210.13179 [cond-mat.dis-nn].

[17] K. Christensen and N. R. Moloney, *Complexity and criticality*, Vol. 1 (World Scientific Publishing Company, 2005).

[18] D. J. Amit and V. Martin-Mayor, *Field theory, the renormalization group, and critical phenomena: Graphs to computers: Third edition* (Field theory, the renormalization group, and critical phenomena: Graphs to computers: Third edition, 2005).

[19] M. Newman and G. T. Barkema, *Monte Carlo Methods in Statistical Physics* (Monte Carlo Methods in Statistical Physics, 1986).

[20] S. Lübeck, Journal of Statistical Mechanics: Theory and Experiment **2006**, P09009 (2006), doi:10.1088/1742-5468/2006/09/p09009.

[21] H. Hinrichsen, Advances in physics **49**, 815 (2000), doi:10.1080/00018730050198152.

[22] M. Henkel, H. Hinrichsen, S. Lübeck, and M. Pleimling, *Non-equilibrium phase transitions*, Vol. 1 (Springer, 2008).

[23] I. Jensen, Journal of Physics A: Mathematical and General **37**, 6899 (2004), doi:10.1088/0305-4470/37/27/003.

[24] M. Munoz, G. Grinstein, R. Dickman, and R. Livi, Physical review letters **76**, 451 (1996), doi:10.1103/physrevlett.76.451.

[25] J. L. Cardy and U. C. Täuber, Journal of statistical physics **90**, 1 (1998), doi:10.1023/A:1023233431588.

[26] J. Cardy and U. C. Täuber, Physical review letters **77**, 4780 (1996), doi:10.1103/physrevlett.77.4780.

[27] J. Carrasquilla and R. G. Melko, Nature Physics **13**, 431 (2017), doi:10.1038/nphys4035.

[28] X. Chen, F. Liu, W. Deng, S. Chen, J. Shen, G. Papp, W. Li, and C. Yang, Physica A: Statistical Mechanics and its Applications **637**, 129533 (2024).

[29] L. Wang, Physical Review B **94**, 195105 (2016), doi:10.1103/physrevb.94.195105.

[30] W. Hu, R. R. P. Singh, and R. T. Scalettar, Phys.rev.e **95**, 062122 (2017), doi:10.1103/physreve.95.062122.

[31] H. K. Janssen, Zeitschrift Für Physik B Condensed Matter **42**, 151 (1981), doi:10.1007/BF01319549.

[32] P. Grassberger, Zeitschrift für Physik B Condensed Matter **47**, 365 (1982), doi:10.1007/BF01313803.

[33] H. Takayasu and A. Y. Tretyakov, Physical Review Letters **68**, 3060 (1992), doi:10.1103/physrevlett.68.3060.

[34] M. H. Kim and H. Park, Physical Review Letters (1994), doi:10.1103/physrevlett.73.2579.

[35] Menyhard and N, Journal of Physics A General Physics **27**, 663 (1994), doi:10.1088/0305-4470/27/3/012.

[36] D. Zhong and D. ben Avraham, Physics Letters A **209**, 333 (1995), doi:10.1016/0375-9601(95)00869-1.

[37] L. Canet, H. Chaté, B. Delamotte, I. Dornic, and M. A. Munoz, Physical review letters **95**, 100601 (2005), doi:10.1103/physrevlett.95.100601.

[38] J. Shen, W. Li, S. Deng, D. Xu, S. Chen, and F. Liu, arXiv preprint arXiv:2112.00489 (2021), doi:10.48550/arXiv.2112.00489.

[39] J. Shen, F. Liu, S. Chen, D. Xu, X. Chen, S. Deng, W. Li, G. Papp, and C. Yang, Physical Review E **105**, 064139 (2022), doi:10.48550/arXiv.2112.15516.

[40] S. Jianmin, L. Wei, D. Shengfeng, and Z. Tao, Physical review. E **103 5-1**, 052140 (2021), doi:10.1103/PhysRevE.103.052140.

[41] E. M. Stoudenmire, Quantum Science and Technology **3**, 034003 (2018), doi:10.1088/2058-9565/aaba1a.

[42] R. Bro and A. K. Smilde, Analytical methods **6**, 2812 (2014), doi:10.1039/C3AY41907J.

[43] M. Wattenberg, F. Viégas, and I. Johnson, Distill **1**, e2 (2016), doi:10.23915/distill.00002.

[44] Y. Wang, H. Yao, and S. Zhao, Neurocomputing **184**, 232 (2016), doi:10.1016/j.neucom.2015.08.104.

[45] H. Andersson and T. Britton, Journal of Mathematical Biology **41**, 559 (2000), doi:10.1007/s002850000060.

[46] D. Mollison, Journal of the Royal Statistical Society. Series B (Methodological) **39**, 283 (1977), doi:10.2307/2985089.

[47] J. P. Bouchaud and A. Georges, Physics Reports **195**, 127 (1990), doi:10.1016/0370-1573(90)90099-N.

[48] H. Hinrichsen, Journal of Statistical Mechanics: Theory and Experiment **2007**, P07006 (2007), doi:10.1088/1742-5468/2007/07/P07006.

[49] U. C. Täuber, *Critical dynamics: a field theory approach to equilibrium and non-equilibrium scaling behavior* (Cambridge University Press, 2014).

[50] J. Zinnjustin, *Quantum Field Theory and Critical Phenomena* (Quantum Field Theory and Critical Phenomena, 1989).

[51] D. J. Amit, *Field theory, the renormalization group, and critical phenomena* (Field theory, the renormalization group, and critical phenomena, 2015).

[52] H. Janssen, K. Oerding, F. van Wijland, and H. Hilhorst, The European Physical Journal B (1999), doi:10.1007/s100510050596.

[53] H.-K. Janssen and U. C. Täuber, Annals of Physics **315**, 147 (2005), doi:10.1016/j.aop.2004.09.011.

[54] H. Hinrichsen and M. Howard, The European Physical Journal B **7**, 635–643 (1999).

[55] X. S. Yang, Luniver Press (2010).

[56] E. Domany and W. Kinzel, Physical Review Letters **53**, 311 (1984), doi:10.1103/PhysRevLett.53.311.

[57] W. Kinzel, Zeitschrift Für Physik B Condensed Matter **58**, 229 (1985), doi:10.1007/BF01309255.